PAPER

Check for updates

Optimized adsorption of volatile organic compounds on graphene oxide and nanoporous graphene activated with ZnCl$_2$: a combined experimental and computational study

Tahereh Zafari,[a] Soheila Sharafinia,[b] Alimorad Rashidi, *[c] Mehdi D. Esrafili,[d] Bahram Keyvani[a] and Mohsen Mousavi[a]

The present research is a comparison study of adsorption capacity of graphene oxide (GO) and nanoporous graphene (NPG) for volatile organic compounds' vapor (here gasoline vapor) adsorption. GO was synthesized using the modified Hummers method. For the synthesis of NPG, a low-cost precursor with unique properties (camphor) was used by the chemical vapor deposition (CVD) method. The effect of reaction temperature parameter, the ratio of camphor to zinc oxide nanocatalyst and reaction time was investigated. The physicochemical properties of the samples were characterized using XRD, FT-IR, Raman, FE-SEM, TEM and BET techniques. It was observed that activation by ZnCl$_2$ at 600 °C and 180 min (*i.e.* NPG2) gives a surface area of 181.61 m^2 g^{-1}. NPG2 showed high adsorption capacity for VOC adsorption (559 mg g^{-1}), which was about 1.34–2.58 times more than other synthesized samples (adsorption capacities of PG1, PG3, GO1, GO2, and GO3 were 415, 310, 300, 367, and 216 mg. g^{-1}, respectively). The high VOC adsorption capacity of PG was due to its $\pi-\pi$ interactions with the NPG surface. Therefore, the NPG2 sample was selected as the best sample. In general, all synthesized samples showed rapid kinetic behaviors for gasoline vapor adsorption, and their maximum adsorption capacity was obtained in the first 35 min. To shed insight on the adsorption process of gasoline on NPG and GO, density functional theory (DFT) calculations were performed. According to the DFT calculations, the adsorption strength of an isobutane (ISO) molecule improved as the pore size on the NPG increased. The adsorption energy of ISO on GO was less than that on NPG, most likely due to steric repulsion between the ISO and O moieties on the GO. The negative enthalpy and Gibbs free energy changes caused by ISO adsorption on NPG and GO showed that the process is thermodynamically favorable at room temperature and pressure.

1. Introduction

In recent years, pollutants produced by the development of industries have had great destructive effects on the environment and the health of humans. Volatile organic compounds (VOCs) are carbon-based chemicals that have characteristics such as high vapor pressure, low boiling point, and high reactivity.[1,2] Factors that produce VOCs include storage and transportation, vehicle exhaust emission, oil refining, oil gas evaporation, disposal of waste materials, *etc.*.[3] According to the literature, about 1.7 L of gasoline is introduced into the environment by gas stations every year.[4]

So far, various methods for the treatment of VOCs such as adsorption,[5] condensation,[6] bio-filtration,[7] membrane separation,[8] catalytic oxidation,[9] degradation reaction,[10,11] and incineration[12] have been introduced to deal with the consequences of VOC emissions. According to US EPA estimates, various adsorbents such as silica gel,[13] zeolites,[14] and AC[7,15] have been used to remove hazardous compounds and VOCs, due to their excellent adsorption capacity, hydrophobicity, thermal stability, and regenerability. Among these materials, carbon-based materials such as graphene materials are considered to be one of the most economical, environmentally friendly, remarkable materials for adsorption of VOCs.[16]

Recently, carbon-based materials play a significant role in nano-technology, and the discovery of graphene is the last of continuous advances in the science of carbon.[17] Graphene is a carbon nanomaterial with a branched hexagonal structure

[a] Department of Chemical Engineering, Saveh Islamic Azad University, Iran

[b] Department of Chemistry, Faculty of Science, Shahid Chamran University of Ahvaz, Ahvaz, Iran

[c] Nanotechnology Research Center, Research Institute of Petroleum Industry (RIPI), Tehran, Iran. E-mail: rashidiam@ripi.ir

[d] Department of Chemistry, Faculty of Basic Sciences, University of Maragheh, Maragheh, Iran

and can act as a two-dimensional building facade for carbon materials (fullerene and nanotubes).[18] Graphene shows many excellent physical, chemical, mechanical and electrical properties. These attributes make it significant for engineering science applications such as photodegradation,[19,20] adsorption,[21–25] catalyst,[26,27] and metrology.[28] Findings have shown that graphene materials have very good efficiency in absorbing many organic pollutants such as VOCs.[29] GO is one of the derivatives of graphene, which is obtained from the oxidation of graphene with various groups containing oxygen such as carboxylic, hydroxyl and epoxide groups.[30] GO-based materials have been widely used to remediate pollutants such as metal ions, radionuclides, dyes, pesticides, and VOCs.[30] Some research studies have shown that modifying the composition of graphene or GO could alter its chemical reactivity, influencing its adsorption attributes onto organic molecules. Graphene has been made by several different methods, one of those methods being CVD.[31]

This study integrates both experimental and computational approaches. The experimental approach involves the synthesis of NPG using the ZnO catalyst (by the CVD method) and then using the ZnCl$_2$ activator to activate the NPGs. These NPGs were investigated for their efficacy in the adsorption of VOC molecules. In parallel, Density Functional Theory (DFT) calculations were performed to gain deeper insight into the molecular-level interactions. The combination of these approaches provides a comprehensive analysis of VOC adsorption and enhances the understanding of the underlying adsorption mechanisms, offering a more robust solution for the development of efficient adsorbents.

On the other hand, the combination of zinc oxide (ZnO) with graphene enhances the adsorptive performance of graphene in various applications. ZnO, due to its semiconducting properties and photocatalytic activity, has a synergistic effect when integrated with graphene. One of the main advantages of this composite is the increase in the active surface area for adsorption. ZnO, with its nanostructured morphology, provides a large surface area that facilitates more effective adsorption of pollutant molecules. Meanwhile, graphene, with its two-dimensional structure and high surface area, serves as an ideal substrate for the uniform dispersion of ZnO nanoparticles. This results in more active sites available for adsorption.[32] In addition, graphene can improve the mechanical and chemical stability of ZnO while also preventing nanoparticle aggregation. This contributes to the overall efficiency and durability of the adsorbent.[32] In summary, the ZnO/graphene composite enhances the adsorption performance by increasing the active surface area and enhancing the structural stability, making it highly effective in removing organic pollutants and heavy metals.

The adsorption kinetics of VOCs by the prepared GO and NPGs were modeled with pseudo-first-order (PFO) and pseudo-second-order kinetic (PSO) models. To gain insightful information about the adsorption strength, dispersion-corrected density functional theory (DFT) calculations were performed.

2. Experimental section

2.1. Materials

The materials used in this study were purchased from Merck (Darmstadt, Germany) and are as follows: ZnO, sulfuric acid (H$_2$SO$_4$, 98%), graphite powder, sodium nitrate (NaNO$_3$), potassium permanganate (KMnO$_4$), hydrogen peroxide (H$_2$O$_2$, 30%), hydrochloric acid (HCl, 37%), and zinc chloride (ZnCl$_2$).

2.2. Instruments

The crystallinity of the samples was determined by X-ray diffraction (XRD) analysis on a Philips PW1800 X-ray diffractometer. The functional groups of the samples were measured using a Fourier transform infrared (FT-IR) spectrometer (Thermos Nicolet AVATAR 360 FT-IR spectrometer in the range of 4000–400 cm^{-1}). Raman spectroscopy (Takram, Teksan Microscope) with a 532 nm wavelength laser source was used in the range of 800–2000 cm^{-1}. Finally, to show the morphology of the samples, Field-Emission Scanning Electron Microscopy (FE-SEM) and Transmission Electron Microscopy (TEM) were exploited to collect images. The BET surface area of the samples was measured using a Micrometrics surface area analyzer (ChemBET-3000, Quantachrome Corp., USA).

2.3. Synthesis of GO

The modified Hummers method[33] was used for the synthesis of GO (Fig. 1). First, 46 mL of H$_2$SO$_4$ was poured into a flask and cooled in an ice bath to 0 °C for 20 min. Then, 1 g of graphite powder and 1 g of NaNO$_3$ were added to the flask and stirred for 30 min. 6 g of KMnO$_4$ was slowly and gradually added to the mixture and stirred at 35 °C for 1 h. Then, 92 mL of deionized water was gently mixed in, and then the temperature was maintained in an oil bath at 100 °C for 15 min. The remaining KMnO$_4$ was gradually removed by adding H$_2$O$_2$. Addition of H$_2$O$_2$ was continued until a gold colored solution formed. Graphite oxide was separated from the solution by filtration and washed with HCl solution (5%). After that, the graphite oxide was washed with deionized water and centrifuged several times. Finally, GO powders were obtained after ultrasonic exfoliation and freeze drying.

2.4. Synthesis of NPG

NPG was synthesized via the CVD method.[34] The CVD technique was utilized on an as-prepared ZnO nano-catalyst in an electrical furnace consisting of a quartz reactor heated up to 900 °C for 1 h. The reaction was proceeded by consuming camphor as the carbon source and hydrogen as the carrier gas. At the end of the reaction, to remove the impurities, the product was washed with HCl (18 wt% w/w) solution and then with hot deionized water to achieve a neutral pH. Eventually, the obtained sample was dried in an oven at 105 °C for 12 h.

2.5. NPG and GO activation with ZnCl$_2$

ZnCl$_2$: NPG with a weight ratio of 3 : 1 was mixed and was placed in an electrical furnace consisting of a quartz reactor
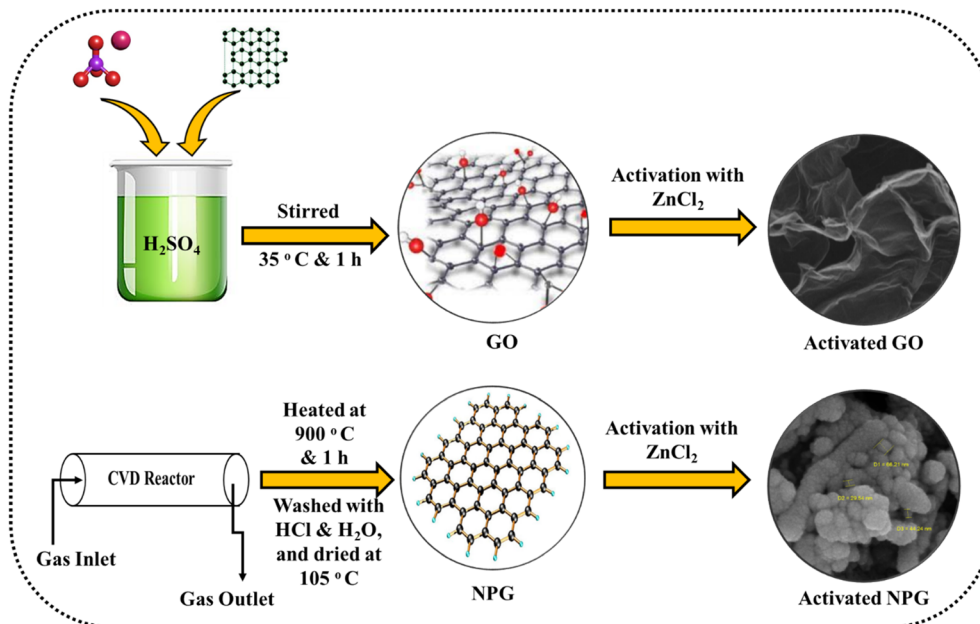
Fig. 1 Schematic image of activated NPG and activated GO preparation.

heated and activated for 3 h under N_2 flow and at a temperature of 500 °C (Fig. 1). Then, the activated NPG was cooled to room temperature and placed in HCl (18 wt%) at ambient temperature. After 24 h, the mixture was filtered and washed with distilled water to neutralize its pH. The resulting powder was dried in an oven at 100 °C for 12 h. The activated NPG was named NPG1. The same method was used for the activation of NPG2, NPG3, GO1, GO2, and GO3, with the difference being the synthesis conditions reported in Table 1.

2.6. DFT calculations

To find out useful information about the adsorption of gasoline on NPG and GO, DFT calculations were performed on some model systems using the DMol3 program. The dispersion-corrected PBE density functional, in combination with the double-numerical plus polarization function (DNP) basis set, was used to optimize these systems. Convergence tolerances of 10^{-5} hartree (Ha), 0.001 Ha Å^{-1}, and 0.005 Å were employed for geometry relaxation, maximum force, and displacement, respectively. The pristine graphene was modeled using a 6×6 supercell with 72 carbon atoms. GO was then prepared by the

addition of oxygen-containing functional groups such as epoxide and hydroxyl to pure graphene. The nanoporous structures were generated by removing carbon atom(s) from graphene or GO. The Hirshfeld charge analysis method was used to determine the charge-transfer values and atomic charges. The formation energy (E_{form}) of NPG surfaces was obtained by the following formula:

$$E_{form} = E_{NG} + n\mu_C - E_G \quad (1)$$

where E_{NG} is the total energy of NPG, E_G is the total energy of pristine graphene, n is the number of removed carbon atoms, and μ_C is the chemical potential of carbon, which is defined as the energy of a carbon atom in pristine graphene. The adsorption energy (E_{ads}) of gasoline was calculated using the following equation:

$$E_{ads} = E_{complex} - E_X - E_S \quad (2)$$

where $E_{complex}$ is the total energy for the adsorbate/substrate complex and E_S and E_X are the energies of the isolated substrate and adsorbate, respectively. The enthalpy (ΔH_{ads}) and Gibbs free energy (ΔG_{ads}) changes due to the formation of complexes were obtained from the thermochemistry calculations by adding thermal (H_{corr}) and Gibbs energy (G_{corr}) corrections to the total electronic energy of these systems, respectively:

$$\Delta H_{ads} = (\varepsilon_0 + H_{corr})_{complex} - (\varepsilon_0 + H_{corr})_X - (\varepsilon_0 + H_{corr})_S \quad (3)$$

$$\Delta G_{ads} = (\varepsilon_0 + G_{corr})_{complex} - (\varepsilon_0 + G_{corr})_X - (\varepsilon_0 + G_{corr})_S \quad (4)$$

where the subscripts complex, X and S refer to the adsorbate/substrate complex, isolated substrate and adsorbate,

Table 1 Activation conditions of NPG and GO with $ZnCl_2$

Sample	Activation temperature/°C	$ZnCl_2$: NPG or GO	Activation time/h
NPG1	500	6	3
NPG2	600	3	3
NPG3	700	9	3
GO1	500	6	3
GO2	600	3	3
GO3	700	9	3

respectively. All the ΔH and ΔG values were calculated at $T = 298.15$ K and $P = 1$ atm.

3. Results and discussion

3.1. Characterization of NPG and GO

Fig. 2 shows the XRD patterns of NPG and GO. The peaks at around $2\theta = 10.5°$ can be associated with graphite oxide (Fig. 2A).[35] The appeared broad peak at 23.5° indicates the crystal plane index C (002) (Fig. 2B), which, in turn, is related to the parallel of the aromatic and carbonized structures.[36] The sharp peak indicates a high degree of orientation. Moreover, the high symmetry of the C (002) peak indicates the absence of γ-bands linked to amorphous and aliphatic structures. Another broad peak is observed at 43.5°, assigned to C (100) diffractions of graphitic and hexagonal carbons,[36] which reflect the size of the aromatic lamina (Fig. 2B), The sharp C (100) peak is an indication of a high degree of aromatic ring condensation.

In order to identify the main functional groups in the structure of GO and NPG, FT-IR spectroscopy was used, and the results are shown in Fig. 3. From the spectrum of GO (see Fig. 3a), different types of oxygen functional peaks related to O–H stretching, C=O stretching and C–O stretching can be seen. The broad peaks at 3445 cm^{-1} and 1583 cm^{-1} belong to the OH groups of water in the compound structure. The existence of two peaks at 2923 cm^{-1} showed sp^3 C–H bonding, which indicated the product was produced in the acidic phase, proving the presence of carboxylic acid in the structure.[37] The readings 1717 cm^{-1} and 1050 cm^{-1} are assigned to C=O and C–O stretching due to carbonyl groups in the product. Comparison of the GO spectrum with the NPG spectrum shows the distinction between their functional groups.[37] The peak at 1717 cm^{-1} in GO vanished, as observed from Fig. 3b, which enlightens the successful detection of the carbonyl group during the reduction process. Besides, graphene peaks observed at 3400.18 cm^{-1} and 1563 cm^{-1} are attributed to the C–OH bond.[37] Hence, confirmation of graphene oxide and graphene structures was validated by the FT-IR study.

In the Raman spectrum (Fig. 4), two significant peaks are observed at 1322 and 1564 cm^{-1} related to the D band and the G band, respectively; the D band originated from the E_{2g}
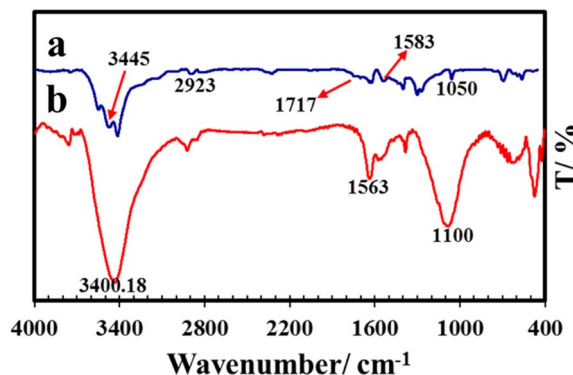

Fig. 3 FTIR spectra of (a) GO and (b) NPG.

vibrational mode of sp^2-hybridized carbon atoms in the graphene lattice, which induced imperfection and disorders, while the G band was from the stretching vibration of sp^2 carbon atoms, related to the first-order distribution.[38] This band indicates the presence of an ordered graphitic structure. A strong D band ($\sim$1322 cm^{-1}) suggests well-structured graphene sheets with fewer defects. This band associated with the breathing modes of aromatic rings, activated by defects or disorder in the sp^2 carbon lattice. The intensity of the D band is directly related to the amount of structural disorder or defects (e.g., edges, vacancies, and functional groups). An increase in the D band indicates more imperfections in the graphene network. The D band to G band intensity ratio (I_D/I_G) is a key parameter to estimate the degree of disorder or defect density in samples. GO exhibits an I_D/I_G ratio of approximately 0.85, indicating a significant amount of structural disorder due to oxygen-containing functional groups disrupting the sp^2 network. The I_D/I_G of NPG (0.94) was greater than that of GO, presenting that the recently formed sp^2 amplitudes after decline were smaller in size but more ordinary.[39]

Fig. 5 indicates the surface morphology of NPG and GO, as determined by FE-SEM and TEM. The FE-SEM image (Fig. 5A) of GO displayed a stacked multilayer sheet structure with a very rough surface. Also, Fig. 5B shows the highly porous structure of NPG with a particle size of about 66.21 nm. Fig. 5C shows the particle size distribution (PSD) of NPG obtained from SEM images. For this purpose, about 40 particles in the image have
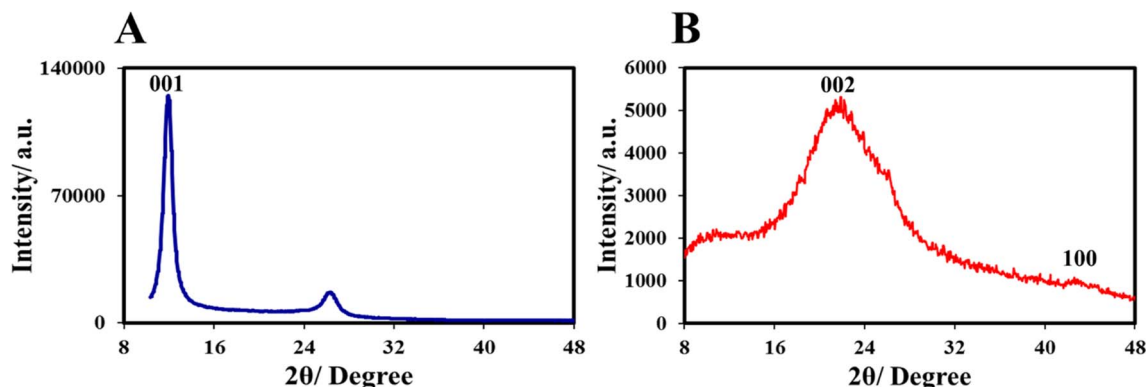

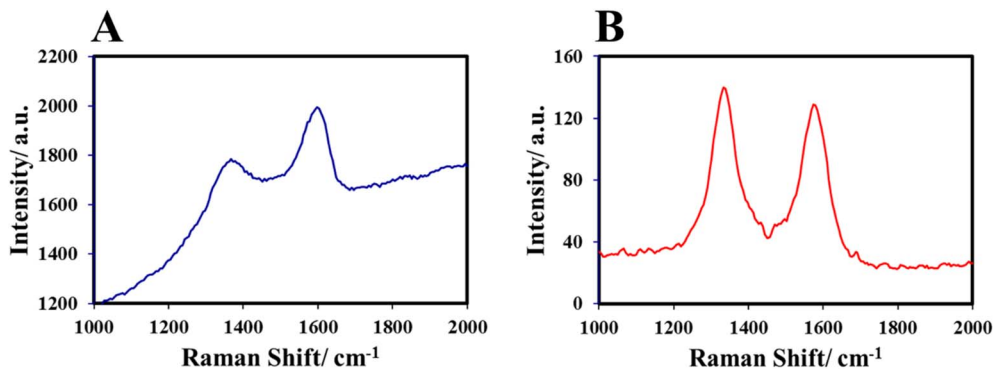Fig. 2 XRD patterns of (A) GO and (B) NPG.

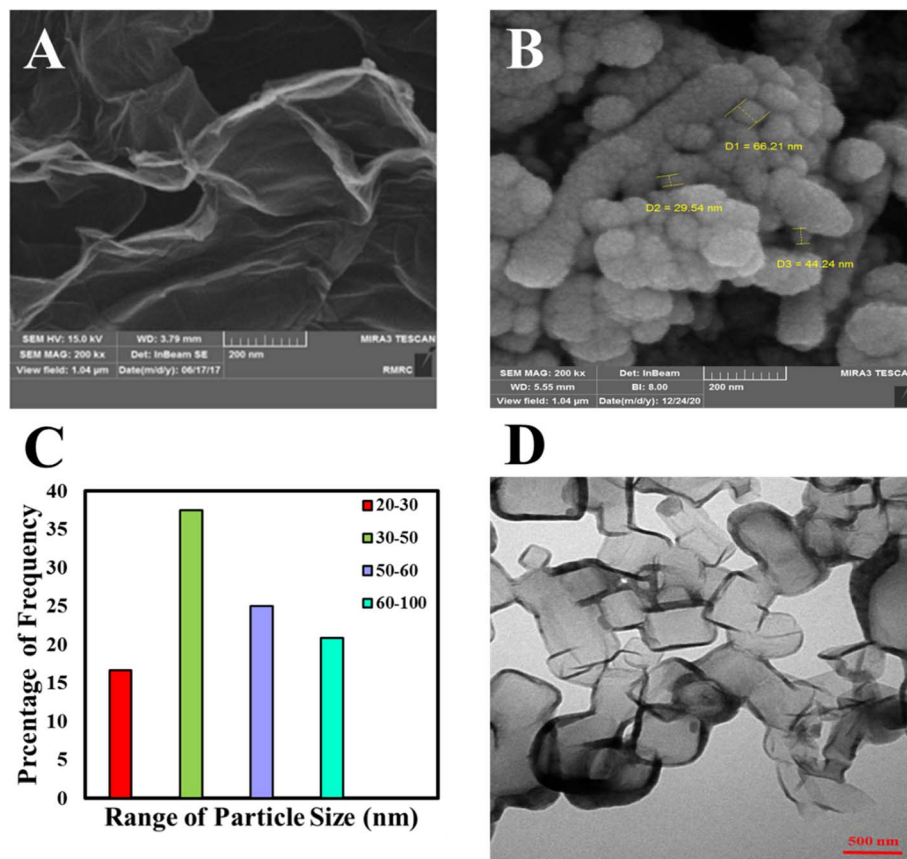Fig. 4   Raman patterns of (A) GO and (B) NPG.

Fig. 5   FE-SEM images of (A) GO and (B) NPG; (C) PSD curve of NPG; (D) TEM image of NPG.

been measured. As can be seen, the most frequent particle size is 30–50 nm, which is due to the presence of micro-molecules of NPG. In Fig. 5D, the TEM image shows the structure of the NPG, which confirms the porous structure of NPG.

Fig. 6 displays the nitrogen adsorption/desorption isotherms at 77 K for NPG. This figure shows that the adsorption of nitrogen on synthesized NPG was acceptably reversible with an obvious hysteresis loop at P/P_o >0.5. According to the IUPAC classification, isotherms shown in Fig. 6A are of type III. Pore diameters are divided into the following categories:[40–42] (i) microspore (pore size < 2 nm), (ii) mesopore (pore size of 2–50 nm), and (iii) macrospore (pore size >50). Since the diameter

pores of the prepared NPG is <2 nm, it has a microporous structure. BJH (Fig. 6B) and BET results and the textural parameters of prepared NPG are presented in Table 2. According to Table 2, NPG had significantly high surface area (181.61 $m^2 g^{-1}$) and pore volume (1.202 $cm^3 g^{-1}$) among the prepared NPGs.

3.2.   Adsorption mechanism of gasoline vapor on NPG and GO

Breakthrough curves for adsorption of gasoline on the prepared GO and NPG are shown in Fig. 7. In this case, the chosen model
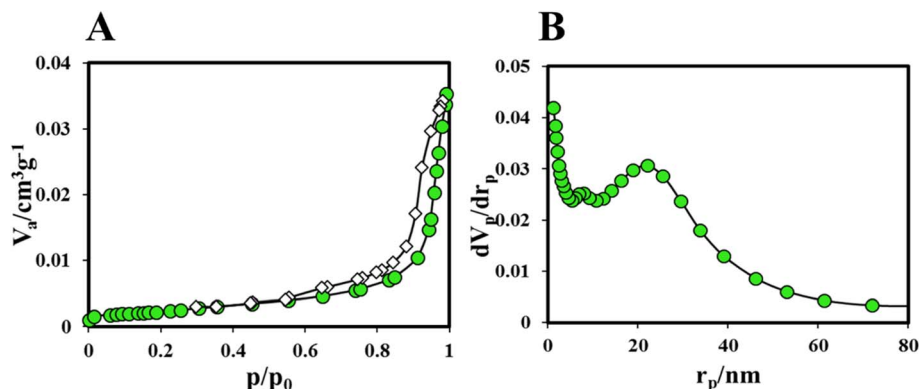
Fig. 6 (A) Nitrogen adsorption/desorption isotherms and (B) BJH plot of NPG.

Table 2 Porous structure parameters of NPGs

Sorbent	BET/m^2 g^{-1}	V_t/cm^3 g^{-1}	Pore volume^{BJH}	Average pore diameter/nm
NPG1	101.2	0.49	0.45	19.42
NPG2	181.61	1.197	1.202	3.477
NPG3	138.91	0.66	0.64	19.15

is gasoline vapor, since ISO is the dominant component of gasoline vapor; therefore, we focus on ISO adsorption – ISO H atoms. Sample NPG2 showed the maximum gasoline adsorption capacity of all samples (Fig. 7A and B). The higher gasoline adsorption capacity (560 mg g^{-1}) of this sample is due to its extremely high pore volume (the ratio of mesopores and microspores). Micro-mesoporous structures improve the adsorption of gasoline and its organic components such as isoparaffinic and natural hydrocarbons, aromatic compounds, and cyclic hydrocarbons with various polarities, shapes, and molecular sizes. In general, the maximum adsorption capacity of all synthesized samples was obtained in the first 35 minutes, so they showed fast kinetic behaviors for gasoline vapor adsorption. The structure of activated NPG led to the diffusion of ISO molecules into the micropores, resulting in adsorption increase.[5,43] In other words, the activation process not only enhances the surface properties of the samples but also has a significant impact on their VOC adsorption capacity. Regarding sensitivity analysis, we found that variations in activation conditions (such as time and temperature) significantly affect the VOC adsorption capacity. In particular, the results showed that increasing the temperature and activation time significantly increases the surface area of the samples, which in turn improves their VOC adsorption capacity. This effect was more pronounced for NPG samples, which have superior surface characteristics compared to NGO. The findings of this study demonstrate that the ZnCl$_2$ activation process significantly influences VOC adsorption capacity, thereby contributing to the optimization process. As shown in Fig. 7, the adsorption capacity is reduced by increasing temperature and mass ratio; it can be due to the destruction of the structure of the pores or functional groups at high temperatures.[43]

Additionally, we evaluated the desorption performance of all samples, which also exhibited outstanding desorption efficiency (Fig. 8). This remarkable adsorption and desorption behavior can be attributed to the suitable surface area, abundant active sites, and the unique porous structure of the nanoporous graphene-based materials, which facilitate efficient capture and release of volatile organic compounds such as gasoline vapor.

3.3. Adsorption kinetics

Adsorption kinetics is a conventional and powerful method to study the effect of time on the adsorption process. In this study, PFO[44,45] and PSO[46] kinetic models were used to investigate the kinetic data. Table 3 shows the linear form of PFO and PSO kinetic models. Using these equations, the values of kinetic parameters of PFO and PSO kinetic models were calculated, and the results are reported in Table 4. Fig. 9 shows that there is a good linear relationship between time (t) and t/q_t. Also, according to the correlation coefficients for the adsorption of ISO by NPG and GO, the value of R^2 for the PFO model is lower than that of the PSO model, so the PSO model is consistent with the adsorption of gasoline by NPG.

3.4. Comparison of the adsorption capacities of GO and NPG studied in this work with other sorbents

As mentioned above, a series of adsorbents from low-cost raw materials were prepared using the CVD method. In this part, a comparison was made between the adsorption capacity of these samples and the samples reported in other research studies, and the results are reported in Table 5. As the table shows, the synthesized samples show high efficiency for VOC adsorption compared to other adsorbents.

4. DFT results

To shed further insight on the adsorption process of gasoline on NPG and GO, detailed DFT calculations on some useful model systems were performed. Because ISO is the major component of gasoline, the adsorption of this molecule is used in the DFT calculations. The optimized geometry of pristine (M1) and four
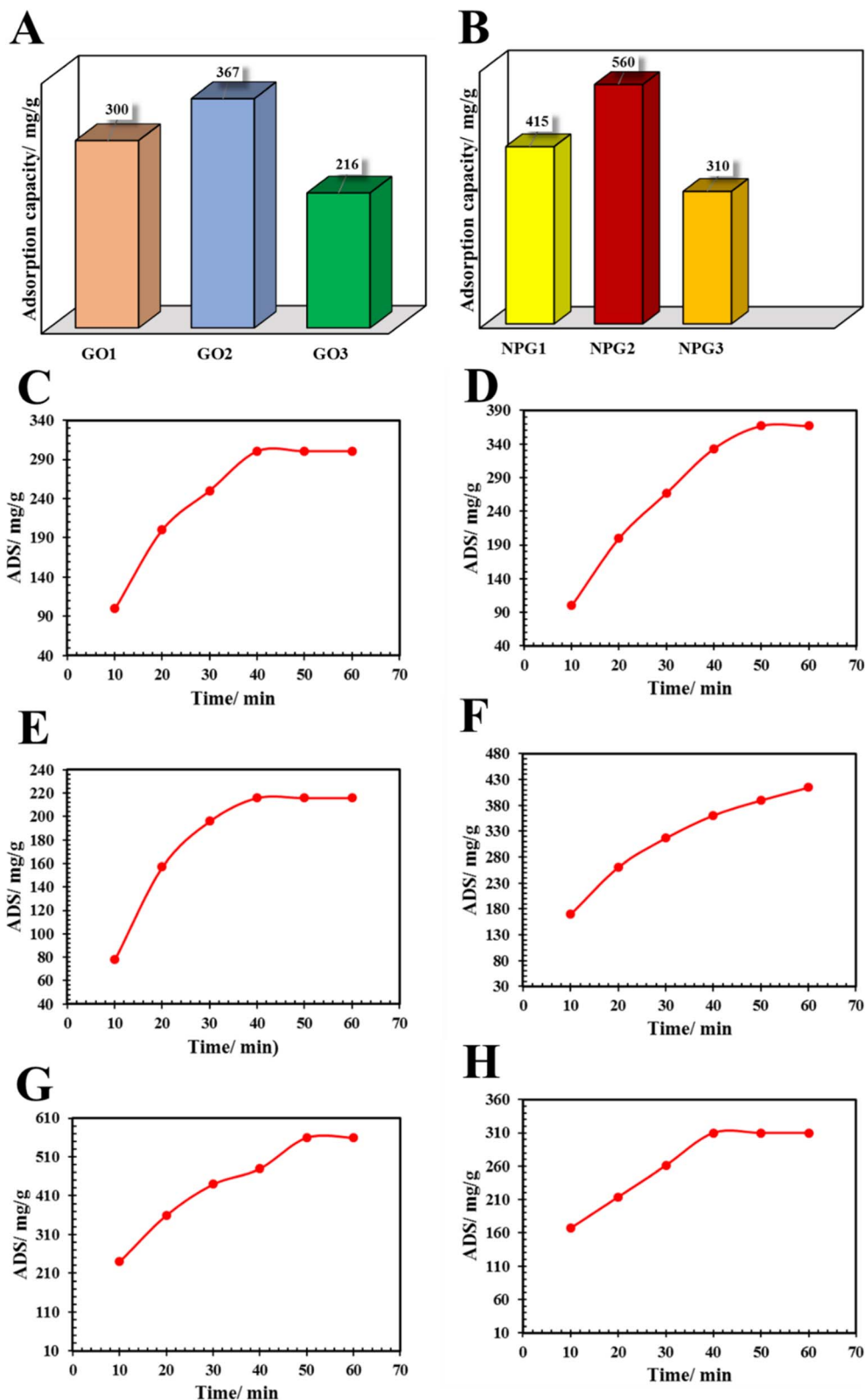
Fig. 7 Adsorption capacity of (A) GO and (B) NGO; ISO adsorption by (C) GO1, (D) GO2, (E) GO3, (F) NPG1, (G) NPG2, and (H) NPG3.

distinct NPG models (M2–M5) employed in this investigation is depicted in Fig. 10. The nanoporous M2–M5 substrates are created by removing one or more carbon atoms from pure graphene and then relaxing the structures. To determine if the formation of such porous structure is thermodynamically favorable, the formation energy (E_{form}) was calculated. Our DFT

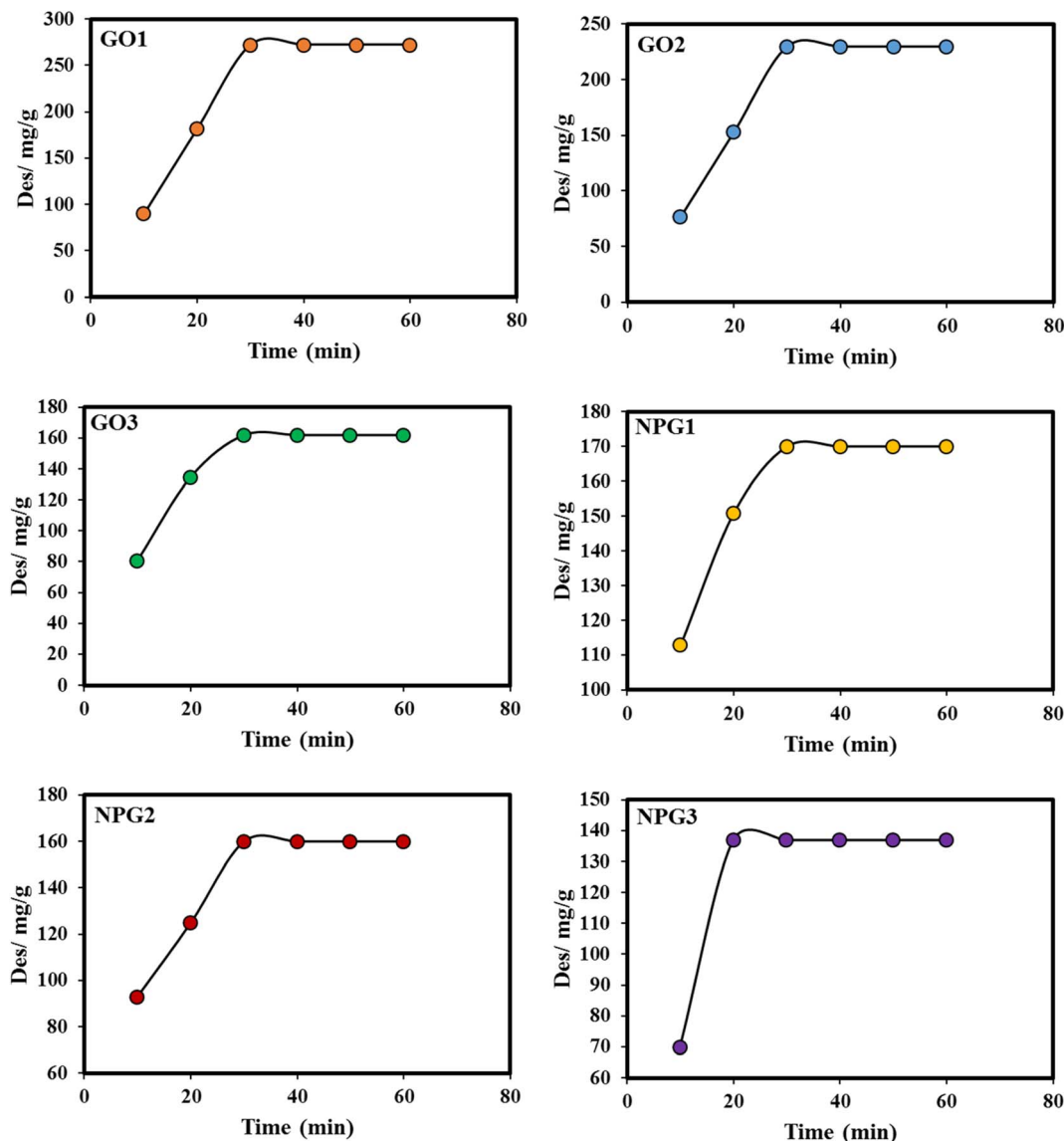Fig. 8   Desorption capacity of GO1, GO2, GO3, NPG1, NPG2, and NPG3.

Table 3   Linear form of each kinetic model

Eq.	Linear form	Parameters	Ref.
PFO	$q_t = q_e[1 - e^{-k_1 t}]$	$q_t/\mathrm{mg\ g^{-1}}$ = Adsorption capacity at t $q_e/\mathrm{mg\ g^{-1}}$ = adsorption capacity at equilibrium $k_1/\mathrm{min^{-1}}$ = PFO rate constant	[5]
PSO	$q_t = \dfrac{k_2 q_e^2 t}{1 + k_2 q_e t}$	$k_2/\mathrm{g\ mg^{-1}}$ min = rate constant of the PSO	[5]

calculations show that the formation of single carbon vacancy defects requires a formation energy of 92 kcal mol^{-1}, which is consistent with previous DFT investigations.[50] Despite the fact that pristine graphene is nonmagnetic, the monovacancy defective graphene has a magnetic moment of 2 μ_B, showing that the existence of a monovacancy defect changes the electronic structure of the graphene substantially. The E_{form} gets more positive as the number of missing carbon atoms increases in graphene, meaning that the formation of the resulting substrates becomes more difficult from a thermodynamic standpoint. Note that the DFT calculations were done at 0 K, and therefore the thermal effects were neglected in the E_{form}. According to molecular dynamics simulations,[51] taking into account such thermal effects might facilitate the formation of

Table 4 Adsorption kinetic parameters for gasoline adsorption onto samples

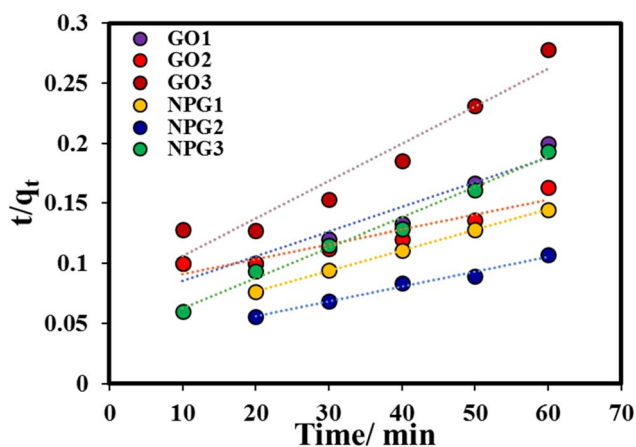| Kinetic model	Adsorbent	Parameters		
		$q_e/\text{mg g}^{-1}$	k_1/min^{-1}	R^2
PFO	GO1	2.69	−0.029	0.95
	GO2	2.78	−0.024	0.97
	GO3	2.63	−0.030	0.95
	NPG1	2.036	−0.014	0.94
	NPG2	2.64	−0.016	0.94
	NPG3	1.89	−0.016	0.99
		$q_e/\text{mg g}^{-1}$	k_2	R^2
PSO				
	GO1	15.384	2.112	1
	GO2	12.820	6.084	0.990
	GO3	13.513	1.335	0.990
	NPG1	23.255	1.849	0.997
	NPG2	32.258	0.384	0.994
	NPG3	27.777	0.648	0.996

Fig. 9 PSO curves for ISO adsorption onto GOs and NPGs.

NPG. As a result, one may assume that the NPGs utilized here are stable at room temperature. According to the Hirshfeld charge density analysis, the charges on the carbon atoms of the NPGs are not uniform. The carbon atoms located around the porous site are mostly negative due to the dangling bonds. As

shown in the following, these should be the most favorable sites for adsorption of ISO molecules. In Fig. 10, we also show the optimized structure of pristine (M6) and nanoporous GO (M7–M10), which is achieved by adding some O-containing functional groups over the graphene sheets. Because the carbon atoms at the defect site are more chemically reactive than others, oxygen moieties are added to these atoms. Based on DFT calculations, the existence of O-containing functional groups reduces the formation energy of defective graphene, making these systems easier to form at room temperature. Because the O atom has a larger electronegativity than carbon, all of the oxygen moieties in the GO substrates are negatively charged. The C atoms surrounding these O atoms, on the other hand, have a substantial positive charge. As a result, significant charge separation occurs between the O and surrounding C atoms, causing some polarity in these systems as compared to NPG substrates. Fig. 11 depicts the optimized structure of an ISO molecule adsorbed over NPG and GO substrates. Table 6 summarizes the adsorption energies (E_{ads}) and amount of charge transferred (Q_{CT}) during ISO adsorption. According to the DFT calculations, ISO is weakly adsorbed on pristine graphene, and its interaction with the carbon atoms is mostly governed by dispersion effects. However, it is found that the ISO is adsorbed on the defect site in NPGs, most likely owing to the buildup of negative charge on the dangling C atoms around the defect sites. The adsorption energy, as provided by eqn (2), was determined to estimate the adsorption strength of ISO. Table 6 shows that all of the E_{ads} values are negative, suggesting that ISO adsorption on NPG surfaces is energetically beneficial. The absolute value of E_{ads} increases in the order M1 < M2 < M3 < M4 < M5, which correspond to the defect size on graphene. This is also well correlated with the average negative charge of the C atoms in these systems. In all situations, a negligible charge is transferred from the ISO to the graphene surfaces, implying that the ISO acts as an electron-donating species in the complexes formed. The E_{ads} values in Table 6, on the other hand, show that the propensity of ISO to adsorb on GO is weaker than that of NPG. This is mainly due to the steric repulsion between the ISO and O moieties on the GO. Also, because ISO behaves as a weak Lewis base on graphene surfaces, the presence of electron-rich O moieties in the GO weakens the charge transfer from the ISO to the substrate.

Table 5 Adsorption capacities of the NPG and GO samples compared with other samples

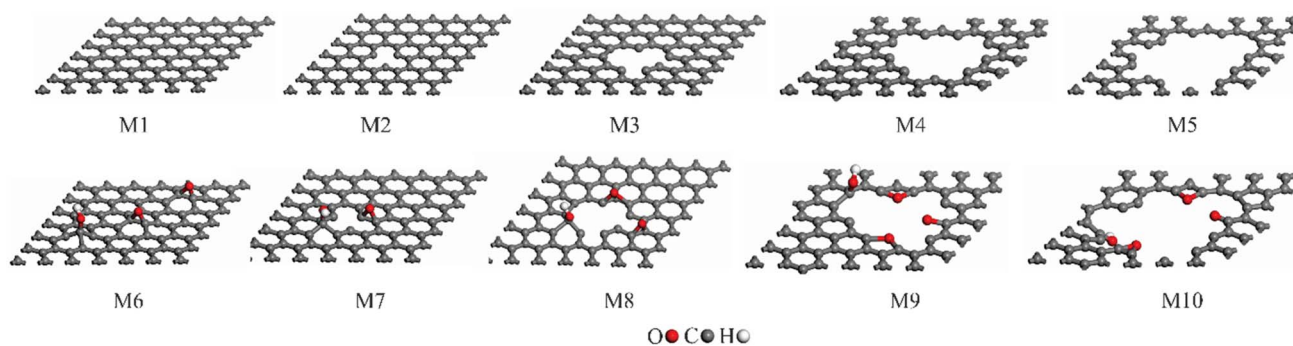| Adsorbent	Adsorbate	Adsorption capacity/mg g^{-1}	Ref.
Activated hydrochar	Acetone	39.42	47
Activated hydrochar	Cyclohexane	121.47	47
CNTs	Toluene	71.27	48
Durian shell activated	Toluene	57.14	49
NPG1	ISO	415	This study
NPG2	ISO	560	This study
NPG3	ISO	310	This study
GO1	ISO	300	This study
GO2	ISO	367	This study
GO3	ISO	216	This study

Fig. 10 DFT optimized geometries of different models used for the pristine graphene (M1), pristine GO (M6), and NPG (M2–M5) and GO (M7–M10).
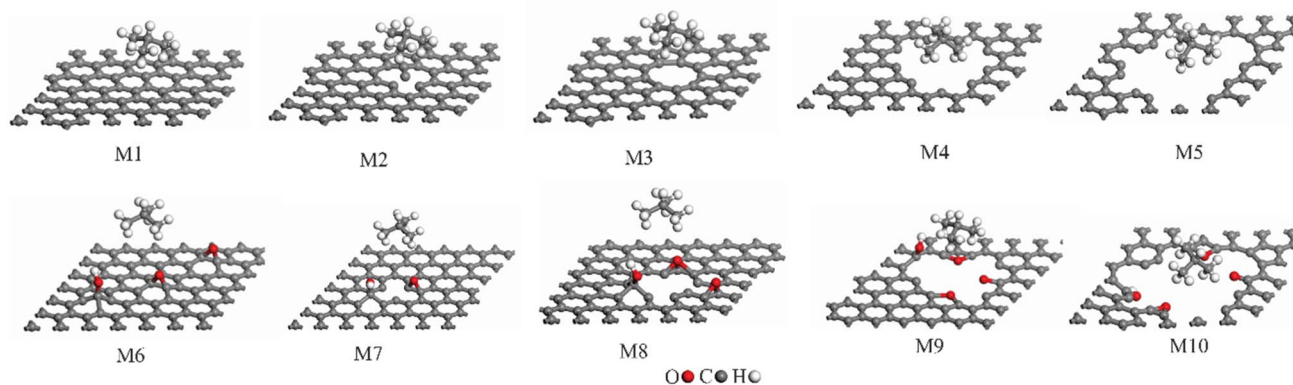

Fig. 11 Optimized geometry of the ISO adsorbed onto different models of NPG and GO.

Table 6 also presents the calculated changes in enthalpy (ΔH_{ads}) and Gibbs free energies (ΔG_{ads}) obtained from the thermochemistry analysis of the optimized structures (at $T = 298.15$ K and $P = 1$ atm). The ΔH_{ads} and ΔG_{ads} values are all negative, showing that ISO adsorption is a thermodynamically favorable process at ambient temperature and pressure. Furthermore, the more negative ΔH_{ads} or ΔG_{ads} values of ISO adsorbed on NPG compared to GO indicate that the adsorption of this molecule is more thermodynamically favorable. It is also

worth noting that the ΔH_{ads} values are less negative than the E_{ads}, implying that thermal effects tend to weaken the adsorption strength of isobutane.

5. Conclusions

In this study, a series of GO and NPG activated with $ZnCl_2$ were successfully synthesized. Then, to evaluate the efficiency of the synthesized samples, the parameters of calcination temperature and the ratio of activator to GO and graphene were optimized, and they were used to adsorption of gasoline vapor. The NPG2 sample showed high adsorption capacity for adsorption of VOC, nearly 1.34–2.58 times more than other synthesized samples. To get further information about gasoline adsorption, dispersion-corrected DFT calculations were performed using different molecular models of NPG and GO. Given that ISO is the primary component of gasoline, the adsorption energies, charge transfers and changes in enthalpy and Gibbs free energy owing to the adsorption of an ISO molecule on different NPG and GO substrates were calculated. DFT calculations indicated that the adsorption energy of an ISO molecule on the NPG is more negative than that on the GO, confirming our experimental findings that gasoline absorption is more favorable on the NPG than on the GO. The changes in enthalpy and Gibbs free energies due to ISO adsorption are all negative, suggesting that this

Table 6 Calculated adsorption energy (E_{ads}, kcal mol^{-1}), charge transfer (Q_{CT}, electrons), and changes in enthalpy (ΔH_{ads}, kcal mol^{-1}) and Gibbs free energy (ΔG_{ads}, kcal mol^{-1}) of ISO adsorbed onto different models of NPG and GO

Substrate	E_{ads}	Q_{CT}	ΔH_{ads}	ΔG_{ads}
M1	−6.82	0.06	−2.18	−0.28
M2	−9.78	0.11	−6.52	−2.06
M3	−11.58	0.13	−8.07	−4.15
M4	−12.80	0.14	−9.56	−5.31
M5	−14.44	0.16	−10.79	−6.77
M6	−7.08	0.07	−2.48	−0.37
M7	−8.25	0.08	−5.82	−1.82
M8	−9.13	0.08	−6.60	−2.44
M9	−9.96	0.09	−7.08	−3.10
M10	−10.27	0.09	−7.64	−3.71

process is thermodynamically favorable at ambient temperature and pressure. Dispersion-corrected DFT calculations revealed that the formation energy in NPG increases as the number of missing carbon atoms increases. The adsorption energy of an ISO molecule over the NPG is less negative than that on the GO, validating our experimental results that gasoline absorption is more favorable on the NPG than on the GO.

Conflicts of interest

The authors declare that they have no known competing financial interests or personal relationships that could have appeared to influence the work reported in this paper.

Data availability

All data generated or analyzed during this study are included in this published article.

Acknowledgements

References

1 Y. Orooji, B. Tanhaei, A. Ayati, S. H. Tabrizi, M. Alizadeh, F. F. Bamoharram, F. Karimi, S. Salmanpour, J. Rouhi and S. Afshar, Heterogeneous UV-Switchable Au nanoparticles decorated tungstophosphoric acid/TiO2 for efficient photocatalytic degradation process, *Chemosphere*, 2021, **281**, 130795.

2 C. Karaman, O. Karaman, P.-L. Show, H. Karimi-Maleh and N. Zare, Congo red dye removal from aqueous environment by cationic surfactant modified-biomass derived carbon: equilibrium, kinetic, and thermodynamic modeling, and forecasting via artificial neural network approach, *Chemosphere*, 2022, **290**, 133346.

3 S. Wang, H. Sun, H.-M. Ang and M. O. Tadé, Adsorptive remediation of environmental pollutants using novel graphene-based nanomaterials, *Chem. Eng. J.*, 2013, **226**, 336–347.

4 M. Hilpert, B. A. Mora, J. Ni, A. M. Rule and K. E. Nachman, Hydrocarbon release during fuel storage and transfer at gas stations: environmental and health effects, *Curr. Environ. Health Rep.*, 2015, **2**, 412–422.

5 S. Sharafinia, A. Rashidi and M. D. Esrafili, Optimized adsorption of volatile organic compounds on the activated carbon prepared from mesquite grain: A combined experimental and computational study, *J. Environ. Chem. Eng.*, 2022, **10**, 108528.

6 T. Virdis, C. Walgraeve, A. Ioannidis, H. Van Langenhove and J. F. Denayer, Multi-component ppm level adsorption of VOCs on the ZIF-8 and UiO-66 MOFs: Breakthrough analysis with selected ion flow tube mass spectrometry, *J. Environ. Chem. Eng.*, 2021, **9**, 106568.

7 W. M. Moe, W. Hu, T. A. Key and K. S. Bowman, Removal of the sesquiterpene β-caryophyllene from air via biofiltration: performance assessment and microbial community structure, *Biodegradation*, 2013, **24**, 685–698.

8 B. Ozturk, C. Kuru, H. Aykac and S. Kaya, VOC separation using immobilized liquid membranes impregnated with oils, *Sep. Purif. Technol.*, 2015, **153**, 1–6.

9 A. H. Bedane, T. X. Guo, M. Eić and H. Xiao, Adsorption of volatile organic compounds on peanut shell activated carbon, *Can. J. Chem. Eng.*, 2019, **97**, 238–246.

10 M. Li, B. Lu, Q.-F. Ke, Y.-J. Guo and Y.-P. Guo, Synergetic effect between adsorption and photodegradation on nanostructured TiO2/activated carbon fiber felt porous composites for toluene removal, *J. Hazard. Mater.*, 2017, **333**, 88–98.

11 A. Rahmaninia, Y. Mansoori, F. Nasiri, A. Bezaatpour and B. Babaei, Surface decorated magnetite nanoparticles with birhodanine and MoO2Cl2 (dmf) 2 as a new magnetic catalyst for epoxidation of olefins, *J. Part. Sci. Technol.*, 2019, **5**, 47–60.

12 K. Rahbar Shamskar, A. Rashidi, P. Aberoomand Azar, M. Yousefi and S. Baniyaghoob, Synthesis of graphene by in situ catalytic chemical vapor deposition of reed as a carbon source for VOC adsorption, *Environ. Sci. Pollut. Res.*, 2019, **26**, 3643–3650.

13 M. Shafiei, M. S. Alivand, A. Rashidi, A. Samimi and D. Mohebbi-Kalhori, Synthesis and adsorption performance of a modified micro-mesoporous MIL-101 (Cr) for VOCs removal at ambient conditions, *Chem. Eng. J.*, 2018, **341**, 164–174.

14 X. Shen, X. Du, D. Yang, J. Ran, Z. Yang and Y. Chen, Influence of physical structures and chemical modification on VOCs adsorption characteristics of molecular sieves, *J. Environ. Chem. Eng.*, 2021, **9**, 106729.

15 S. Sharafinia, A. Rashidi, A. Ebrahimi, B. Babaei, M. H. Hadizadeh, M. D. Esrafili and M. Pourkhalil, Enhanced VOCs adsorption with UIO-66–porous carbon nanohybrid from mesquite grain: A combined experimental and computational study, *Sci. Rep.*, 2024, **14**, 25177.

16 X. Zhang, B. Gao, A. E. Creamer, C. Cao and Y. Li, Adsorption of VOCs onto engineered carbon materials: A review, *J. Hazard. Mater.*, 2017, **338**, 102–123.

17 A. C. Ferrari, Raman spectroscopy of graphene and graphite: Disorder, electron–phonon coupling, doping and nonadiabatic effects, *Solid State Commun.*, 2007, **143**, 47–57.

18 A. K. Geim and K. S. Novoselov, The rise of graphene, *Nat. Mater.*, 2007, **6**, 183–191.

19 M. Liu, Y. Wang, Y. Chen, T. Zhang, Z. Zhang, H. Li, F. Shan and T. Ma, Anti-stacking, recyclable and electron-rich Fe3O4 modified L-glutamic acid functionalized graphene oxide towards Cr (VI) removal by adsorption-reduction behavior, *Sep. Purif. Technol.*, 2025, 132090.

20 M. P. da Silva, A. C. A. de Souza, Á. R. D. Ferreira, P. L. A. do Nascimento, T. J. M. Fraga, J. V. F. L. Cavalcanti, M. G. Ghislandi and M. A. da Motta Sobrinho, Synthesis of superparamagnetic Fe3O4–graphene oxide-based material

for the photodegradation of clonazepam, *Sci. Rep.*, 2024, **14**, 18916.

21 D. D. Justino, M. O. Alves, B. R. Galvão, R. Santamaría, F. B. De Sousa and P. F. Ortega, The effects of functionalization on graphene oxide for organic dye adsorption: An experimental-theoretical study using electronic structure calculations and statistical mechanical modeling, *J. Mol. Liq.*, 2023, **387**, 122612.

22 T. J. M. Fraga, M. G. Ghislandi, M. N. Carvalho and M. A. da Motta Sobrinho, One step forward: How can functionalization enhance the adsorptive properties of graphene towards metallic ions and dyes?, *Environ. Res.*, 2020, **184**, 109362.

23 T. J. M. Fraga, M. A. da Motta Sobrinho, M. N. Carvalho and M. G. Ghislandi, State of the art: synthesis and characterization of functionalized graphene nanomaterials, *Nano Express*, 2020, **1**, 022002.

24 T. J. Fraga, M. N. Carvalho, M. G. Ghislandi and M. A. d. Motta, Functionalized graphene-based materials as innovative adsorbents of organic pollutants: A concise overview, *Braz. J. Chem. Eng.*, 2019, **36**, 1–31.

25 N. S. Tadayoni, M. Dinari and A. Torbatian, Novel flower-like magnetic core-shell covalent triazine polymer as a beneficial Direct Scarlet 4BS adsorbent and comprehensive study of the kinetics and isotherm adsorption, *J. Environ. Chem. Eng.*, 2023, **11**, 110647.

26 N. Shekarlab, R. Ghorbani-Vaghei and S. Alavinia, Preparation and characterization of copper/ polysulfonamide complex immobilized on geraphene oxide as a novel catalyst for the synthesis of pyrimido [1, 2-a] benzimidazoles, *Appl. Organomet. Chem.*, 2020, **34**, e5918.

27 S. Koosha, R. Ghorbani-Vaghei and S. Alavinia, Copper-anchored polysulfonamide-modified UiO-66-NH2/sodium alginate nanocatalyst for sustainable synthesis of 1, 2, 3-triazoles, *Nanoscale Adv.*, 2025, **7**(7), 1937–1945.

28 S. Deng, V. Tjoa, H. M. Fan, H. R. Tan, D. C. Sayle, M. Olivo, S. Mhaisalkar, J. Wei and C. H. Sow, Reduced graphene oxide conjugated Cu2O nanowire mesocrystals for high-performance NO2 gas sensor, *J. Am. Chem. Soc.*, 2012, **134**, 4905–4917.

29 G. Zhao, L. Jiang, Y. He, J. Li, H. Dong, X. Wang and W. Hu, Sulfonated graphene for persistent aromatic pollutant management, *Adv. Mater.*, 2011, **23**, 3959–3963.

30 L. Zhu, D. Shen and K. H. Luo, A critical review on VOCs adsorption by different porous materials: Species, mechanisms and modification methods, *J. Hazard. Mater.*, 2020, **389**, 122102.

31 C. Mattevi, H. Kim and M. Chhowalla, A review of chemical vapour deposition of graphene on copper, *J. Mater. Chem.*, 2011, **21**, 3324–3334.

32 V. Venkidusamy, S. Nallusamy, G. Nammalvar, R. Veerabahu, A. Thirumurugan, C. Natarajan, S. S. Dhanabalan, D. P. Pabba, C. V. Abarzúa and S.-K. Kamaraj, Zno/graphene composite from solvent-exfoliated few-layer graphene nanosheets for photocatalytic dye degradation under sunlight irradiation, *Micromachines*, 2023, **14**, 189.

33 C. Xia, Y. Li, T. Fei and W. Gong, Facile one-pot synthesis of superhydrophobic reduced graphene oxide-coated polyurethane sponge at the presence of ethanol for oil-water separation, *Chem. Eng. J.*, 2018, **345**, 648–658.

34 A. Rashidi, K. J. Jozani, M. Pourkhalil, M. Mohajeri, H. Ghorbani and M. Rashtchi, Highly-ordered Nanostructure Arrays and Methods of Preparation Thereof, *US Pat.* 9446951, U.S. Patent and Trademark Office, Washington, DC, 2016.

35 C. Rao, K. Biswas, K. Subrahmanyam and A. Govindaraj, Graphene, the new nanocarbon, *J. Mater. Chem.*, 2009, **19**, 2457–2469.

36 S. Ramanathan, S. Moorthy, S. Ramasundaram, H. K. Rajan, S. Vishwanath, S. Selvinsimpson, A. Durairaj, B. Kim and S. Vasanthkumar, Grape seed extract assisted synthesis of dual-functional anatase TiO2 decorated reduced graphene oxide composite for supercapacitor electrode material and visible light photocatalytic degradation of bromophenol blue dye, *ACS Omega*, 2021, **6**, 14734–14747.

37 M. Aziz, F. A. Halim and J. Jaafar, Preparation and characterization of graphene membrane electrode assembly, *J. Teknol.*, 2014, **69**, 11–14.

38 J. Wang, Z. Chen and B. Chen, Adsorption of polycyclic aromatic hydrocarbons by graphene and graphene oxide nanosheets, *Environ. Sci. Technol.*, 2014, **48**, 4817–4825.

39 S. Stankovich, D. A. Dikin, R. D. Piner, K. A. Kohlhaas, A. Kleinhammes, Y. Jia, Y. Wu, S. T. Nguyen and R. S. Ruoff, Synthesis of graphene-based nanosheets via chemical reduction of exfoliated graphite oxide, *Carbon*, 2007, **45**, 1558–1565.

40 S. Sharafinia, A. Farrokhnia, E. G. Lemraski and A. Rashidi, Magnetic perovskite nanohybrid based on g-C3N4 nanosheets for photodegradation of toxic environmental pollutants under short-time visible irradiation, *Sci. Rep.*, 2023, **13**, 21323.

41 S. Sharafinia, A. Farrokhnia, E. G. Lemraski and A. Rashidi, Decoration of ZnFe2O4 and UiO-66 over g-C3N4 as magnetically novel reusable visible light photocatalyst for degradation of Rh–B, *Opt. Mater.*, 2022, **132**, 112838.

42 S. Sharafinia, R. Halladj and A. Rashidi, Significant enhancement of nitrogen photofixation to ammonia and hydrogen storage by a MIL-53 (Fe) based novel plasmonic nanocatalysis at ambient condition, *Sci. Rep.*, 2025, **15**, 12010.

43 J. Binner, *Advanced Materials 1991-1992: I. Source Book*, Elsevier, 2013.

44 S. Sharafinia, A. Rashidi, F. Tabarkhoon, F. Dehghan, F. Tabarkhoon and M. Bazmi, Effective adsorption of amoxicillin by using UIO-66@ Cr-MIL-101 nanohybrid: isotherm, kinetic, thermodynamic, and optimization by central composite design, *Sci. Rep.*, 2023, **13**, 22689.

45 S. Sharafinia and A. Rashidi, MIL-101 (Cr) hybrid nanoporous carbon derived MOF as a nano-adsorbent for dye removal using RSM-CCD, *Arabian J. Chem.*, 2023, **16**, 105288.

46 E. G. Lemraski, S. Yari, E. K. Ali, S. Sharafinia, H. Jahangirian, R. Rafiee-Moghaddam and T. J. Webster,

Polyvinyl alcohol/chitosan/silver nanofibers as antibacterial agents and as efficient adsorbents to remove methyl orange from aqueous solutions, *J. Iran. Chem. Soc.*, 2022, **19**, 1287–1299.

47 X. Zhang, W. Xiang, B. Wang, J. Fang, W. Zou, F. He, Y. Li, D. C. Tsang, Y. S. Ok and B. Gao, Adsorption of acetone and cyclohexane onto CO2 activated hydrochars, *Chemosphere*, 2020, **245**, 125664.

48 Y. Sun and P. A. Webley, Preparation of activated carbons from corncob with large specific surface area by a variety of chemical activators and their application in gas storage, *Chem. Eng. J.*, 2010, **162**, 883–892.

49 Y. Tham, P. A. Latif, A. Abdullah, A. Shamala-Devi and Y. Taufiq-Yap, Performances of toluene removal by activated carbon derived from durian shell, *Bioresour. Technol.*, 2011, **102**, 724–728.

50 S. Haldar, R. G. Amorim, B. Sanyal, R. H. Scheicher and A. R. Rocha, Energetic stability, STM fingerprints and electronic transport properties of defects in graphene and silicene, *RSC Adv.*, 2016, **6**, 6702–6708.

51 K. Yoon, A. Rahnamoun, J. L. Swett, V. Iberi, D. A. Cullen, I. V. Vlassiouk, A. Belianinov, S. Jesse, X. Sang and O. S. Ovchinnikova, Atomistic-scale simulations of defect formation in graphene under noble gas ion irradiation, *ACS Nano*, 2016, **10**, 8376–8384.